Multiscale motion analysis of the carotid artery wall from B-mode ultrasound: investigating the optimal wavelet parameterization

N. N. Tsiaparas, *Student Member, IEEE*, A. Gastounioti, *Student Member, IEEE*, S. Golemati, *Member, IEEE*, and K. S. Nikita, *Senior Member, IEEE*

***Abstract*—The incorporation of wavelet-based multiscale image decomposition in motion-estimation schemes has been shown to have a favourable impact on accuracy in tracking motion of the carotid artery wall from B-mode ultrasound image sequences. In this work, in an attempt to further enhance accuracy, we investigate the effects of different parameters of multiscale image decomposition. To this end, we optimize multiscale weighted least-squares optical flow (MWLSOF), a previously presented multiscale motion estimator, in terms of (a) the type of wavelet transform (WT) (discrete (DWT) and stationary (SWT) WTs), (b) the WT function and (c) the total number of levels of image decomposition. The optimization is performed in the context of an *in silico* data framework, consisting of simulated ultrasound image sequences of the carotid artery. We propose SWT, a high-order coiflet function (ex. coif5) and one level of multiscale image decomposition as the optimal parameterization for MWLSOF to achieve maximum accuracy in the particular application. Finally, we demonstrate the usefulness of an accurate motion estimator in real data experiments, by applying the optimized MWLSOF to real image data of patients with carotid atherosclerosis.**

I. Introduction

Arterial wall motion during the cardiac cycle can be estimated from B-mode ultrasound by recording image sequences and, subsequently, applying motion estimation algorithms to the successive frames of the image sequences. Several studies on the wall-lumen interface and within the tissue [1], adjacent arterial layers [2], proximal and distal arterial walls [3], and atherosclerotic plaques [4] have shown that motion estimators can adequately characterize the arterial wall motion from ultrasound image sequences.

Multiscale motion estimation additionally includes the decomposition of the images of a sequence using multiscale transforms. Multiscale motion estimation has been shown to be superior to the standard approach for motion estimation (i.e. direct application of motion algorithms to the image sequences), probably because it provides information about motion structures at different resolutions and scales. Specifically, the combination of conventional motion estimators with wavelet-based multiscale image analysis has significantly enhanced their accuracy in estimating radial and longitudinal displacements of the carotid artery wall; multiscale versions of block matching [5], affine optical flow [6] and weighted least-squares optical flow (WLSOF) [7] yielded average error reductions up to 70%, 9% and 14%, respectively. However, the discrete wavelet transform (DWT) used in these studies has a major disadvantage, which may limit the potential of multiscale motion estimation; DWT is shift variant, i.e. the wavelet coefficients of the original image and its shifted versions differ.

Based on the above, the purpose of this paper is to optimize multiscale motion estimation in terms of multiscale procedures. To this end, the multiscale version of WLSOF (MWLSOF) [7] was used, because WLSOF has been shown to outperform other motion estimators [8] and MWLSOF has been most effective among the investigated multiscale motion estimators [5]-[7]. In the context of an *in silico* data framework, MWLSOF was optimized in terms of (a) the wavelet transform (WT), by comparing the DWT and the stationary WT (SWT), (b) the WT function and (c) the total number of levels of image decomposition. The optimized MWLSOF was then applied to real ultrasound image sequences of patients with carotid atherosclerosis.

II. Material & Methods

A. Multiscale Weighted Least-Squares Optical Flow

WLSOF is a differential algorithm, which estimates a pixel's velocity using the pixels in a local neighborhood, assuming that they share the same velocity. A detailed presentation of the algorithm and the parameterization that assures maximal accuracy in motion tracking is available in [8]. MWLSOF is based on the combination of WLSOF with multiscale image analysis using a 2-dimensional (2D) WT [7].

The 2D WT of an image is defined as two successive WTs, firstly on the rows of the image and then on the columns of the resulted image. The decomposition of the image yields four subimages at the first level (j=1), namely an approximation subimage A_1 and the horizontal, vertical,

Manuscript received July 25, 2013; accepted September 9, 2013. This work was supported in part by the Operational Program "Competitiveness and Entrepreneurship" and Regional Operational Programmes of the National Strategic Reference Framework (NSRF) 2007-2013. "SYNERGASIA": "Collaborative projects of small and medium scale". The work of A. Gastounioti was also supported in part by a scholarship from the Hellenic State Scholarships Foundation.

N. N. Tsiaparas, A. Gastounioti and K. S. Nikita are with the National Technical University of Athens, Biomedical Simulations and Imaging Laboratory, 9 Iroon Politechniou Str, Athens, Greece. (phone: +30 210 7722968; fax: +30 210 7722320; e-mails: ntsiapar@biosim.ntua.gr, gaimilia@biosim.ntua.gr, knikita@ece.ntua.gr).

S. Golemati is with the 1st Intensive Care Unit, Medical School, National & Kapodistrian University of Athens, Athens, Greece (e-mail: sgolemati@med.uoa.gr).

978-1-4799-3163-7/13/$31.00 ©2013 IEEE

and diagonal detail subimages Dh_1, Dv_1, and Dd_1, respectively. Each subimage is the result of a convolution with two half-band filters; two lowpass filters for A_1, a lowpass and a highpass for Dh_1, a highpass and a lowpass for Dv_1, and two highpass filters for Dd_1. At the next, and each subsequent, level, only the approximation subimage is further decomposed into new four suimages. The total number of levels L depends on the size of the original image; the maximum value of L is equal to $min\ (log_2N, log_2M)$, where N is the number of rows and M is the number of columns. The WT is called DWT if, at every level, convolution with filters is followed by downsampling; otherwise the WT is called SWT (see [9] for more details).

Briefly, MWLSOF consists of the following steps [7]: (1) The images of a sequence are decomposed up to L levels using a 2D WT. (2) A pixel is selected as a target in the first image of the sequence of original images. (3) WLSOF is initially performed at the highest decomposition level L and the radial, rad_L, and longitudinal, $long_L$, positions of the target are estimated. (4) For every lower decomposition level j, with $0 \leq j < L$, measurements of rad_j and $long_j$ are obtained by performing WLSOF at that level. The final measurements for level j are estimated by combining rad_j and $long_j$, with rad_{j+1}, and $long_{j+1}$. This step gradually leads to the final estimates for $j=0$ (rad_0 and $long_0$), which also correspond to the final motion estimates. (5) The final rad_j and $long_j$ for $0 < j \leq L$ are updated by appropriately scaling rad_0 and $long_0$.

B. In Silico Optimization of Multiscale Procedures

As explained before, DWT and SWT both yield four (approximation, horizontal, vertical, and diagonal) subimages at each level of image decomposition. MWLSOF can be implemented by using either one of them or all four subimages. Preliminary studies have showed that maximum accuracy for MWLSOF, using DWT, is achieved when the approximation subimages are used [7]. Given that this choice also significantly reduces the computational cost of SWT, the approximation subimages were selected in this study, too.

DWT-based MWLSOF has achieved optimal performance for $L=1$ [7]. This study investigated whether this choice is also optimal for SWT. However, the main optimization of MWLSOF concerned the type of WT (i.e. DWT or SWT) and the WT function.

In terms of the WT function, 49 alternatives were investigated. The criteria that were used to select these functions included the compact support (filters with finite support), the existence of a scaling function (which is produced by a low pass filter) and the orthogonality (which allows fast discrete transformed implementation). Therefore, crude and infinitely regular WT functions, such as Gaussian, Morlet, Mexican hat and Meyer, were excluded. Only orthogonal (Daubechy, coiflet, symlet) and biorthogonal/reverse biorthogonal WT functions were used. Among them, and by taking the size of the original images into consideration, WT functions produced by filters with higher than 30 samples were also excluded. The remaining WT functions have different properties, i.e. vanishing moments (order), symmetry, length and parity of their filters (Table 1).

Table 1: Properties of wavelet functions. VM: vanishing moments; LP-L: length of low-pass filter; HP-L: length of high-pass filter; PR: parity of filter (1 odd, 2 even); SM: Symmetry of the filter (0 no, 1 near, 2 yes). Wavelet family: db: Daubechy, sym: symlet, bior: biorthogonal, coif: coiflet, rbio: reverse biorthogonal.

No.	Abbreviation	VM	LP-L	HP-L	PR	SM
1	db1 (haar)	1	2	2	2	2
2	db2	2	4	4	2	0
3	db3	3	6	6	2	0
4	db4	4	8	8	2	0
5	db5	5	10	10	2	0
6	db6	6	12	12	2	0
7	db7	7	14	14	2	0
8	db8	8	16	16	2	0
9	db9	9	18	18	2	0
10	db10	10	20	20	2	0
11	sym1	1	2	2	2	1
12	sym2	2	4	4	2	1
13	sym3	3	6	6	2	1
14	sym4	4	8	8	2	1
15	sym5	5	10	10	2	1
16	sym6	6	12	12	2	1
17	sym7	7	14	14	2	1
18	sym8	8	16	16	2	1
19	sym9	9	18	18	2	1
20	sym10	10	20	20	2	1
21	coif1	1	6	6	1	1
22	coif2	2	12	12	2	1
23	coif3	3	18	18	2	1
24	coif4	4	24	24	2	1
25	coif5	5	30	30	2	1
26	bior2.2	2.2	5	3	1	2
27	bior2.4	2.4	9	3	1	2
28	bior2.6	2.6	13	3	1	2
29	bior2.8	2.8	17	3	1	2
30	bior3.1	3.1	4	4	2	2
31	bior3.3	3.3	8	4	2	2
32	bior3.5	3.5	12	4	2	2
33	bior3.7	3.7	16	4	2	2
34	bior3.9	3.9	20	4	2	2
35	bior4.4	4.4	9	7	1	2
36	bior5.5	5.5	9	11	1	2
37	bior6.8	6.8	17	11	1	2
38	rbior2.2	2.2	3	5	1	2
39	rbior2.4	2.4	3	9	1	2
40	rbior2.6	2.6	3	13	1	2
41	rbior2.8	2.8	3	17	1	2
42	rbior3.1	3.1	4	4	2	2
43	rbior3.3	3.3	4	8	2	2
44	rbior3.5	3.5	4	12	2	2
45	rbior3.7	3.7	4	16	2	2
46	rbior3.9	3.9	4	20	2	2
47	rbior4.4	4.4	7	9	1	2
48	rbior5.5	5.5	11	9	1	2
49	rbior6.8	6.8	11	17	1	2

The optimization of MWLSOF was performed in the context of an *in silico* data framework, consisting of 6 simulated image sequences of the carotid artery, for which ground-truth is available [8]. Briefly, the first image sequence (S_0) was simulated by deforming a real image of the carotid artery of a young subject. Four additional image sequences were generated, by adding different levels of Gaussian (S_{G25} and S_{G15}) or speckle (S_{SP25} and S_{SP15}) noise. The sixth image sequence was simulated using an ultrasound simulation package, which incorporates realistic transducer features. Approximately 200 motion targets were selected for

each image sequence and accuracy in motion estimation was evaluated using the warping index, defined as the mean geometric error, in pixels, between the ground-truth and the estimated displacements for all motion targets [8].

C. Real Data Application

In an attempt to demonstrate the significant role of an accurate motion estimator in studying the mechanical behavior of the arterial wall, the optimized version of MWLSOF was applied to B-mode ultrasound image sequences of the carotid artery of an asymptomatic and a symptomatic patient with established carotid atherosclerosis. Carotid arteries were imaged in longitudinal sections (Fig. 1), using the following scanner settings: dynamic range, 75 dB; persistence, low; and frame rate, 33 frames/s. MWLSOF was used to produce radial strain (RS) waveforms which represent local deformations (i.e. ratios of change in radial distance to initial radial distance) between (a) healthy parts of the anterior and posterior walls (RS at wall) and (b) the top and bottom surfaces of the plaque (RS at plaque) [8].

Figure 1: First frames of ultrasound image sequences for (a) an asymptomatic and (b) a symptomatic patient with carotid atherosclerosis. The outlines of the atherosclerotic plaques are marked in white colour.

III. Results & Discussion

Figure 2 shows bar plots of mean, over all WT functions, warping indices produced by MWLSOF for varying L values, using either SWT or DWT. In all cases, the amount of energy in approximation images reduces as L increases; hence, similarly to DWT [7], the lowest warping indices for SWT were obtained for L=1.

Table 2 presents mean ± standard deviation, minimum and maximum, over all WT functions, warping indices produced by MWLSOF for L=1, using either SWT or DWT. In general, SWT produced statistically lower indices than DWT. This is probably associated with the limitation posed by the DWT's shift-variant property. Exceptions were observed for S_{G25} and S_{G15}. This might be due to the type of noise added on the sequences; high frequency noise is concentrated on the detail subimages of the first level of image decomposition and the downsampling procedure of DWT probably results in the elimination of a high amount of noise components.

According to Table 2, the lowest warping index for each image sequence was obtained by a high-order WT function. In contrast, the highest warping indices were obtained by a low-order WT function. The order of the WT function provides information about the degree of polynomials used to represent images; the higher the order, the better the representation of complex images. The order is also entirely determined by the length of the lowpass filter, with high-order WT functions resulting in appropriate damping of the oscillations of its coefficients out of the region of interest.

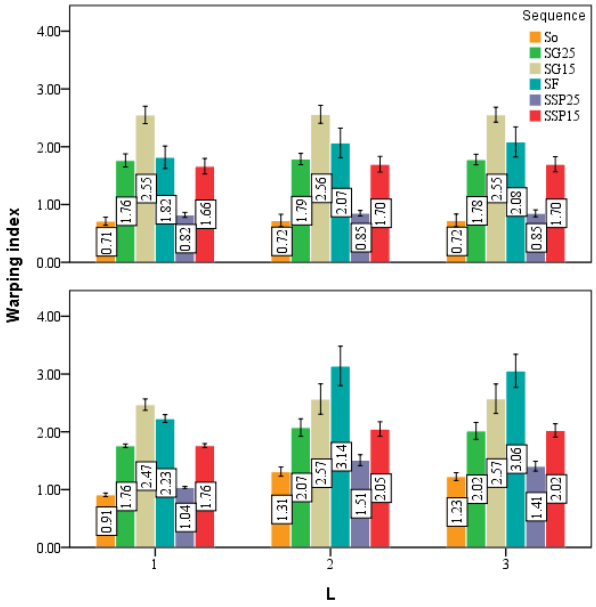

Figure 2: Bar plots of mean, over all wavelet functions, warping indices (in pixels) produced by MWLSOF for varying levels of image decomposition (L=1, 2, 3), using either SWT (top) or DWT (bottom). T – lines represend mean values in ± 3 standard deviations.

Table 2: Warping indices, in pixels, produced by MWLSOF for 1 level of image decomposition, using either SWT or DWT for each image sequence. The presented values correspond to mean ± standard deviation, over all wavelet functions, warping indices. Minimum and maximum warping indices (and the corresponding wavelet functions) are also presented for each case.

	DWT			SWT		
	mean ±std	min (wavelet)	max (wavelet)	mean ±std	min (wavelet)	max (wavelet)
S_0	0.91 ±0.01	0.87 (db10)	0.91 (bior3.9)	0.71 ±0.02*	**0.67** (sym10)	0.75 (db1)
S_{G25}	1.76 ±0.01	**1.67** (bior3.1)	1.78 (bior3.5)	1.76 ±0.04	1.70 (db9)	1.81 (db2)
S_{G15}	2.47 ±0.03	**2.38** (db10)	2.51 (rbio5.5)	2.55 ±0.05	2.46 (rbior3.9)	2.64 (db1)
S_F	2.23 ±0.02	2.17 (db10)	2.27 (bior3.1)	1.82 ±0.06*	**1.73** (bior3.9)	1.98 (db1)
S_{SP25}	1.04 ±0.01	1.01 (db10)	1.04 (bior3.1)	0.82 ±0.01*	**0.8** (db8)	0.85 (bior3.1)
S_{SP15}	1.76 ±0.13	1.73 (db9)	1.78 (bior3.3)	1.66 ±0.04*	**1.57** (coif5)	1.74 (bior3.1)

* Significantly different compared to DWT (t-test, $p<0.001$).
Boldface indicates lowest warping index values for each image sequence.

General linear models and univariate procedures for each image sequence, and SWT for one level of image decomposition, were used to define the main effects of the length of lowpass filter, its parity and symmetry on warping indices (Table 3). The length of highpass filter was excluded due to high correlation with the lowpass filter. No statistically significant effects were found for the parity and symmetry properties. In contrast, as expected, there was a high association between the warping index and the length of the lowpass filter in each model.

Table 3: Statistical significance (p-value) after univariate analysis of variance for SWT and 1 level of image decomposition for each image sequence; LP-L: length of low-pass filter.

	S_0	S_{G25}	S_{G15}	S_F	S_{SP25}	S_{SP15}
Symmetry	0.467	0.415	0.793	0.629	0.507	0.813
Parity	0.589	0.800	0.289	0.166	0.197	0.262
LP-L	<0.001	<0.001	<0.001	0.003	<0.001	<0.001

Table 4 shows the mean, over all WT functions of each wavelet family, warping indices produced by SWT-based MWLSOF for L=1. The coiflet family produced the lowest values for most of the sequences. Considering the results of Tables 2 and 4, a high-order coiflet WT function, ex. coif5 which produced lowest warping indices for S_{SP15}, is proposed as the most suitable choice for SWT-based MWLSOF. Figure 3 illustrates the superiority, in terms of accuracy in motion tracking, of this optimal version of MWLSOF (i.e. using SWT for coif5 and L=1) with respect to WLSOF [7].

Table 4: Mean, over all functions of a wavelet family, warping indices, in pixels, produced by MWLSOF for 1 level of image decomposition using SWT.

	S_o	S_{G25}	S_{G15}	S_F	S_{SP25}	S_{SP15}
coiflet	**0.71**	**1.74**	**2.52**	1.83	0.82	**1.63**
Daubechy	**0.71**	1.75	2.54	1.83	**0.81**	1.66
symlet	0.72	1.78	2.57	1.83	0.82	1.68
biorthogonal	**0.71**	1.77	2.57	**1.80**	0.83	1.68
reverse biorthogonal	0.72	1.77	2.54	1.82	0.82	1.65

Boldface indicates the lowest value for each image sequence.

Figure 4 presents the RS waveforms which were generated from the application of the optimized MWLSOF to real ultrasound image data. All waveforms exhibited distinct periodic patterns, while RS at plaque seems to synchronize with RS at wall for both patients. Moreover, with respect to the asymptomatic patient, the symptomatic one demonstrated RS at plaque of higher amplitude; the opposite was observed for RS at wall. Such observations reveal deformations which occur within the wall and may have a significant effect on the vulnerability of atherosclerotic lesions.

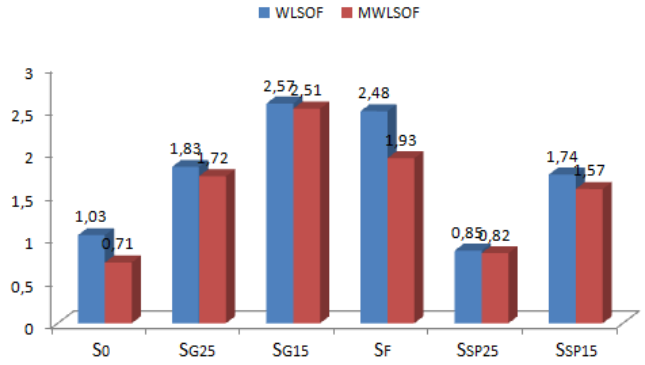

Figure 3: Warping indices (in pixels) produced by WLSOF and the optimized version of MWLSOF.

IV. Conclusion

This study demonstrated that different parameters of multiscale image decomposition have a significant impact on the accuracy of multiscale motion estimators in tracking motion of the carotid artery wall from B-mode ultrasound images. Multiscale image analysis using SWT and a high-order WT function for 1 level of image decomposition compose the optimal parameterization. Specifically, among wavelet families, high-order coiflet functions (ex. coif 5) are proposed as more suitable for the particular application.

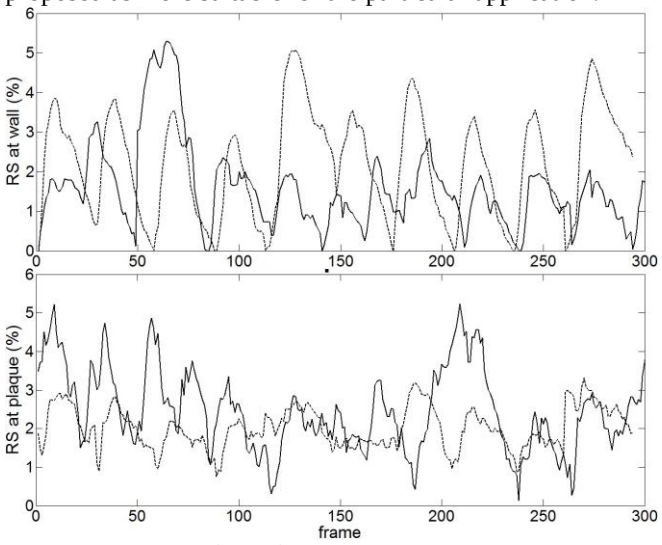

Figure 4: Strain waveforms for an asymptomatic (dotted line) and a symptomatic (solid line) patient with carotid atherosclerosis.

References

[1] S. Golemati, A. Sassano, M. J. Lever, A. A. Bharath, S. Dhanjil, and A. N. Nicolaides, "Motion analysis of carotid atherosclerotic plaque from B-mode ultrasound," *Ultrasound Med. Biol.*, vol. 29, no. 3, pp. 387–399, Mar. 2003.

[2] M. Cinthio, A. R. Ahlgren, J. Bergkvist, T. Jansson, H. W. Persson, and K. Lindström, "Longitudinal movements and resulting shear strain of the arterial wall," *Am J Physiology – Heart Circul. Physiol.*, vol. 291, no. 1, pp. H394–H402, Jul. 2006.

[3] G. Zahnd, L. Boussel, A. Marion, M. Durand, P. Moulin, A. Sérusclat, D. Vray, "Measurement of two-dimensional movement parameters of the carotid artery wall for early detection of arteriosclerosis: a preliminary clinical study," *Ultrasound Med. Biol.*, vol. 37, no. 9, pp. 1421-1429, Sep. 2011.

[4] T. Dahl, J. Bang, A. Ushakova, S. Lydersen, and H. O. Myhre, "Parameters describing motion in carotid artery plaques from ultrasound examination: a reproducibility study," *Ultrasound Med. Biol.*, vol. 30, no. 9, pp. 1133–1143, Sep. 2004.

[5] A. Gastounioti, N.N. Tsiaparas, S. Golemati, and K.S. Nikita, "Multiscale block matching for carotid artery wall motion estimation from B-mode ultrasound", *7th GRACM International Congress on Computational Mechanics*, Athens, Greece, June 30-July 2, 2011.

[6] A. Gastounioti, N.N. Tsiaparas, S. Golemati, J.S. Stoitsis, and K.S. Nikita, "Affine optical flow combined with multiscale image analysis for motion estimation of the arterial wall from B-mode ultrasound", *33rd Annual International Conference of the IEEE Engineering in Medicine and Biology Society (EMBC'11)*, Boston, MA, USA, August 30 - September 3, 2011, pp. 559-562.

[7] A. Gastounioti, S. Golemati, N.N. Tsiaparas, J.S. Stoitsis, K.S. Nikita, "Multiscale approach for weighted least-squares optical flow for estimating arterial wall displacements", *10th IEEE International Workshop on Biomedical Engineering (10th BioEng)*, October 5 - 7, 2011, Kos island, Greece.

[8] S. Golemati, J.S. Stoitsis, A. Gastounioti, A.C. Dimopoulos, V. Koropouli, K.S. Nikita, "Comparison of block-matching and differential methods for motion analysis of the carotid artery wall from ultrasound images," *IEEE Trans. Inf. Technol. Biomed.*, vol. 16, no. 5, pp. 852-858, Sep. 2012.

[9] N. N. Tsiaparas, S. Golemati, I. Andreadis, J. S. Stoitsis, I. Valavanis, K. S. Nikita, "Comparison of multiresolution features for texture classification of carotid atherosclerosis from B-mode ultrasound," *IEEE Trans. Inf. Technol. Biomed.*, vol. 15, no. 1, pp. 130–137, 2011.